International Journal for Housing Science and Its Applications
Publish August 10, 2025. Volume 46, Issue 4 Pages 7605-7618

https://doi.org/10.70517/ijhsa464655

Research on the Optimization of Slope Critical Soil Layer Thickness Algorithm and Landslide Risk Assessment by Integrating FLAC-3D and GIS

Lida Wang[1], Yuqiong He[1], Yongqi Wang[1,*] and Yunxi Zhao[1]
[1] Faculty of Transportation Engineering, Kunming University of Science and Technology, Kunming, Yunnan, 650500, China
Corresponding authors: (e-mail: wanglida@stu.kust.edu.cn).

Abstract Slope stability analysis has always been a core issue in the field of geotechnical engineering. However, the distribution of soil layers in slopes exhibits natural spatial variability due to factors such as sedimentation, making it impossible to accurately characterize their true distribution using limited borehole data alone, thereby hindering precise evaluation of their stability. A model was constructed using the strength reduction method combined with numerical simulation, employing the Ball-Wall method for modeling, to analyze the critical soil layer thickness for the stability of terraced slopes. Six factors—bulk density, cohesion, internal friction angle, slope angle, slope height, and pore water pressure ratio—were selected as model inputs. A slope stability prediction model based on the improved Northern Eagle Algorithm-optimized Random Forest (INGO RF) was proposed, and the optimized machine learning model was compared and analyzed with other models. The results indicate that the thicker the fully weathered soil layer, the lower the slope stability coefficient. After 5 days of rainfall, the stability coefficients under different soil layer conditions are not significantly different. However, in the absence of rainfall, slopes with thinner fully weathered soil layers are significantly more stable. The optimal INGO RF model achieved an accuracy rate greater than 0.9 on both the training and testing datasets. After comparing the predictive performance of various models, it was found that the INGO RF model outperforms other models, with bulk density being the most sensitive factor influencing slope stability.

Index Terms strength reduction method, slope stability, soil layer thickness, random forest, improved Northern Goshawk optimization algorithm

I. Introduction

With the development of society, an increasing number of large-scale engineering projects have emerged worldwide, giving rise to various types of slopes. These primarily include rock slopes formed by the weathering of rock masses, soil particle slopes created by the accumulation of soil from mining activities, and mixed rock-soil slopes, among others [1]-[3]. Rock slopes are composed of structural planes and structural bodies. Structural planes divide rock masses into irregularly shaped and variably sized rock blocks, thereby forming structural bodies [4]. Structural planes are geological interfaces formed within rock masses under tectonic stress, exhibiting directionality, high extensibility, and low thickness as two-dimensional surfaces. Due to their complex structure and significant role in engineering, the stability of such slopes is primarily influenced by joint distribution characteristics, water seepage forces, and external loads such as earthquakes, making them a research hotspot in the field of civil engineering in recent years [5]-[7]. Soil particle accumulation slope soils are relatively loose and fragmented, formed by the stacking and bonding of soil particles. Under the combined effects of long-term rainfall and self-weight, they possess a certain strength, with porosity smaller than that of sandy soils. Such slopes have poor stability, primarily influenced by water seepage forces, their own porosity, upper pressure loads, and external loads such as earthquakes and explosions [8]-[11].

Slope instability issues are widely present in fields such as geotechnical engineering, environmental science, and transportation. Slopes may become unstable due to factors such as geological structural damage, rainfall erosion, earthquakes, and impact forces, leading to landslides that cause significant economic losses to society and pose a serious threat to human life. This highlights the importance of slope structural stability for engineering structural safety [12]-[15]. Therefore, studying slope instability issues holds significant theoretical and scientific significance. As a core indicator for evaluating slope stability, the critical soil layer thickness is closely related to the severity of disasters caused by slope instability [16]. Discussing the principles and critical values of instability without

considering the actual thickness of the critical soil layer is unreasonable. Analyzing the critical soil layer thickness and predicting stability during slope instability is of great importance.

Currently, research on the critical soil layer thickness for slope instability is still in its early stages. Literature [17] proposed a theoretical model supported by a stress characteristic method and pseudo-static method to analyze the critical stability of pure clay slopes under seismic conditions. The critical slip surface in this environment resembles that under natural conditions but is steeper and lower compared to traditional linear slopes. Reference [18] monitors critical displacements of slopes, integrates slope mechanics, physical information, and deformation behavior to analyze slope failure mechanisms, and develops a dynamic risk prediction method for slopes that have not reached critical values. Machine learning algorithms have made significant contributions to slope stability prediction. Literature [19] combines machine learning algorithms with Winsorization for slope stability prediction. Winsorization enhances prediction performance, with the Random Forest + Winsorization combination yielding the best prediction performance, while Support Vector Machine + Winsorization improves prediction accuracy by nearly 20%. Literature [20] compared the predictive performance of the Gravity Search Algorithm, Random Forest, Support Vector Machine, and Naive Bayes for slope stability. The first two algorithms performed better, with the Gravity Search Algorithm yielding the optimal predictive results. Literature [21] combined an improved Pelican Optimization Algorithm with the Random Forest Algorithm to design a slope stability prediction indicator system, construct a slope stability prediction model, and achieve an accuracy rate of 90.4%. Literature [22] designed a neural network architecture guided by dimensionless indicator groups, combined relative curvature radius and numerical calculations to analyze slope stability, and trained artificial neural networks to achieve three-dimensional slope stability prediction. Literature [23] used digital twin technology and convolutional neural networks to construct a database of slopes with weak layers and predict the stability of slopes with weak layers, achieving a prediction accuracy of up to 95.4%.

This paper will conduct stability simulation calculations for clay slopes using the strength reduction method, combined with the numerical simulation software PFC to establish a computational model. The Ball-Wall method will be employed for modeling to analyze the impact of critical soil layer thickness on the stability of terraced slopes. The following parameters are selected as the primary indicators influencing slope instability: soil density, cohesion, internal friction angle, slope angle, slope height, and pore pressure ratio. A slope stability prediction model based on the Improved Northern Eagle Algorithm-optimized Random Forest (INGO RF) is proposed. The classification performance of INGO RF was evaluated using confusion matrix metrics, characteristic curves, and area under the curve, and the optimized INGO RF model was compared with other models.

II. Analysis of critical soil layer thickness for slope instability

II. A. Strength reduction method approach and model construction

II. A. 1) Strength reduction method

The shear strength reduction method [24] uses the reduction coefficient F_r to reduce the shear strength indicators of the soil, namely cohesion c and internal friction angle φ, according to Equations (1) and (2). The reduced shear strength parameters are substituted for the original shear strength parameters to obtain the new shear strength of the soil τ_{fF}, as shown in Equation (3):

$$c_F = c / F_r \tag{1}$$

$$\varphi_F = \arctan((\tan\varphi) / F_r) \tag{2}$$

$$\tau_{fF} = \frac{c + \sigma \tan\varphi}{F_r} = c_F + \sigma \tan\varphi_F \tag{3}$$

In the equation: c_F is the cohesion of the soil after strength reduction, φ_F is the internal friction angle of the soil after strength reduction, and τ_{fF} is the shear strength of the soil after strength reduction.

In the limit equilibrium method, the stability safety factor K of a slope is defined as the ratio of the shear strength within the slope to the shear stress generated within the soil, as shown in Equation (4):

$$K = \frac{\tau_f}{\tau} = \frac{c + \sigma \tan\varphi}{\tau} \tag{4}$$

Dividing both sides of equation (4) by K yields:

$$\frac{\frac{\tau_f}{K}}{\tau} = \frac{\frac{c + \sigma \tan\varphi}{K}}{\tau} = 1 \tag{5}$$

By comparing Equations (3) and (5), it can be seen that the shear strength reduction factor is equivalent to the slope stability safety factor in the limit equilibrium method.

To ensure that the problem is initially close to elastic, the value of the reduction factor F_r should be sufficiently small at this stage. Subsequently, the reduction factor F_r is gradually increased, causing the shear strength index of the slope to decrease progressively until it reaches a certain value that triggers the instability of the entire soil mass. The shear strength coefficient F_r immediately preceding the onset of overall instability is the stability safety factor of the slope.

At present, there are mainly the following methods to judge whether the soil slope has reached the critical failure: (1) numerical calculation of convergence or not is used as the evaluation criterion, (2) the displacement inflection point of the characteristic part is used as the evaluation criterion, and (3) whether the continuous zone is developed in the soil as the evaluation criterion. In the Abaqus environment, the parameters of the material can be changed with temperature or field variables to achieve this strength reduction process.

The specific steps are as follows:

(1) Define the field variable (strength reduction coefficient F_r).

(2) Define the simulation parameters of the material as a function of the field variable.

(3) In the initial stage, first determine the magnitude of the field variables, apply the physical load to the model, and set the equilibrium stress state. The initial stage is naturally to avoid model failure, so the reduction coefficient F_r needs to be set to a relatively small value. If $F_r < 1$, the shear strength of the slope will be amplified.

(4) In subsequent analyses, the field variable values gradually increase linearly. When the calculation is paused (due to numerical divergence), the results are processed.

II. A. 2) Model Construction

The model in this paper uses a homogeneous soil slope with a height of $12m$ and a slope angle of 45°. The density of the soil is $20kN \cdot m^{-3}$, the cohesion c is $12.38kPa$, and the internal friction angle φ is 20°. Here, the elastic modulus is assumed to be $100MPa$ and the Poisson's ratio is 0.35. The model is shown in Figure 1.

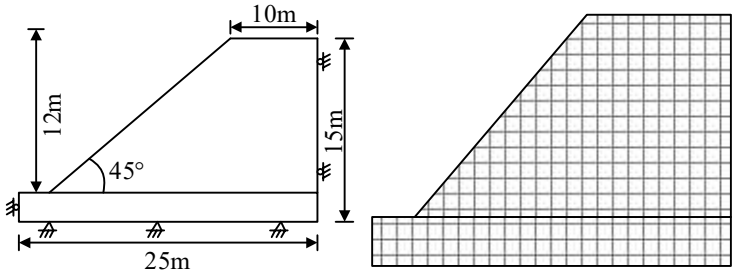

(a) Theoretical model (b) Numerical model

Figure 1: Model drawing

II. B.Establishment of a numerical model for landslides

There are typically two methods for establishing PFC landslide models. One method uses wall elements to simulate the slip surface, while the slip body is filled with particle elements. This modeling method is referred to as the Ball-Wall method. The other method is the ball-ball method, where particle elements are used to fill both the slip body and the slip surface. Based on field investigations and relevant data, the potential sliding surface of the Zhulin Gou landslide has been identified. Additionally, since the Ball-Wall method requires fewer particles, computational efficiency is significantly improved. Therefore, the Ball-Wall method will be adopted for modeling. The modeling process is as follows:

(1) First, using the geological cross-section diagram of the slope, create a slope geometric model of the same dimensions using AutoCAD.

(2) In PFC, use commands such as geometry import and wall import to import the previously generated geometric model into PFC and generate the corresponding wall boundaries.

(3) Use the expansion method to generate particles with the corresponding porosity within the walls, and perform multiple trial calculations to achieve equilibrium under gravitational force. The initial landslide model is shown in Figure 2.

(4) Assign relevant parameters to the generated soil particles, and finally delete the corresponding boundary walls of the landslide body. Since the stress between particles after wall deletion will cause particles to separate extensively, an additional iteration equilibrium must be performed to ensure that the maximum unbalanced contact

force of particles approaches 0, indicating that the entire model system has reached a balanced state, as shown in Figure 3.

(5) Reset the velocity and displacement of the landslide model. Apply gravity to the model using the set gravity command to cause the model to slide under gravitational force. The slope contour line serves only as a reference for slope sliding.

The established numerical calculation model is shown in Figure 4, with a length of 530 m, a height of 210 m, a slope of approximately 20°, a minimum particle radius of 0.08 m, and a maximum particle radius of 0.11 m.

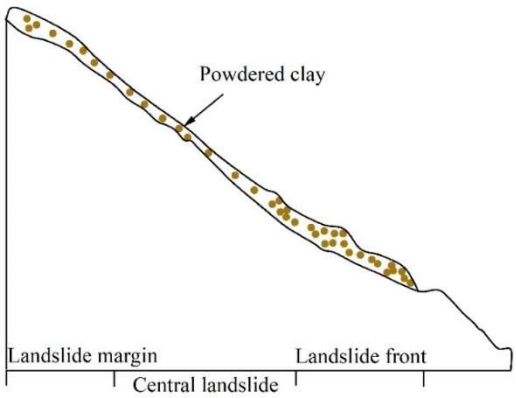

Figure 2: Landslide initial model

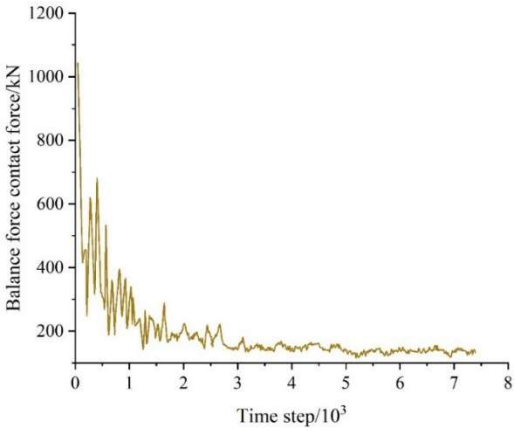

Figure 3: Unbalanced force diagram

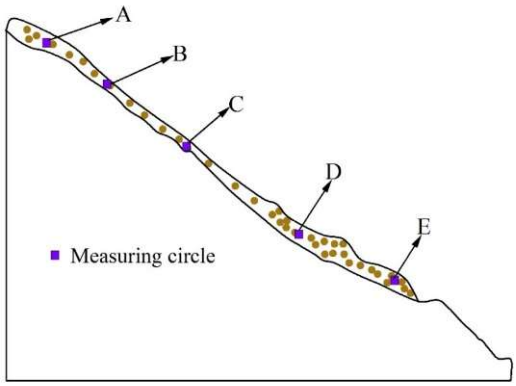

Figure 4: Numerical slope model

II. C.Critical soil layer thickness analysis

Monitoring points were selected at the crest and toe of each terrace to analyze changes in pore water pressure, with the results shown in Figure 5. (a) and (b) represent the slope crest and slope toe, respectively. As shown in the figure: the amplitude of pore water pressure changes at the slope crest decreases with increasing thickness of the fully weathered soil layer, but the rate of decrease gradually slows down. At the slope toe, under conditions where the thickness of the fully weathered soil layer is 1 m and 2 m, the time to reach zero pore pressure is 4 days, 4.7 days at 3 m, and 5 days at both 4 m and 5 m. This indicates that as the influence of rainfall seepage increases, a thinner fully weathered soil layer means the soil is more easily converted from an unsaturated state to a saturated state, allowing the wetting front to reach the slope toe more quickly. As shown in Figure 5, the magnitude of the increase in pore water pressure over time at the slope crest and toe is negatively correlated with soil layer thickness. Under identical conditions, a thicker fully weathered soil layer results in greater rainfall infiltration depth and a longer time required for the wetting front to reach the slope toe. Therefore, in the scenario with a fully weathered soil layer thickness of 5m, the magnitude of pore water pressure changes at the slope crest is smaller than in other scenarios.

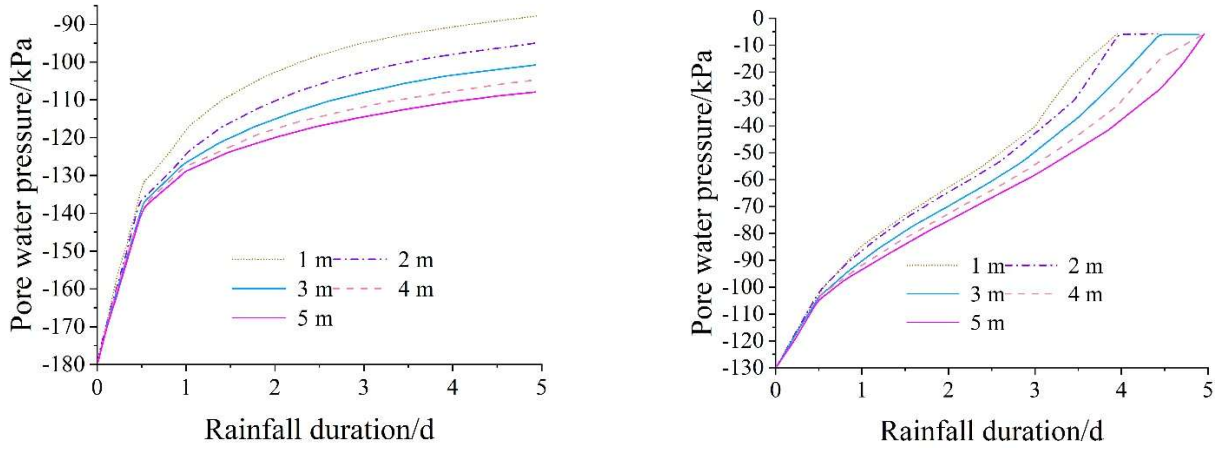

(a) Sloping top (b) Slope

Figure 5: The variation curve of pore pressure force in different soil thickness terraced land

The relationship curves showing how the slope stability coefficient of terraced fields varies over time under different soil layer thickness conditions, as calculated using the unsaturated limit equilibrium method, are shown in Figure 6. As can be seen from the figure: Under no rainfall conditions, the stability coefficient of terraced slopes with the same terrace width and terrace height decreases as the thickness of the fully weathered soil layer increases. During rainfall, the stability coefficients under all conditions first remain unchanged and then decrease as the duration of rainfall increases. Among these, the stability coefficients of terraced slopes with thinner fully weathered soil layers (1–3 m) begin to decrease earlier than those of slopes with thicker layers (4–5 m).

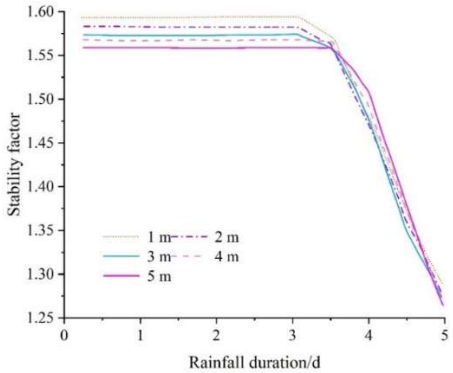

Figure 6: The slope stability coefficient of the slope of the slope of different layers of soil

The changes in the stability of terraced slopes with varying soil layer thicknesses after 5 days of rainfall are shown in Table 1. As shown in Figures 5 and 6: the stability coefficient of the terraced fields decreases with the increase in the thickness of the fully weathered soil layer. Under various conditions, the stability coefficients of the terraced field slopes after 5 days range from 1.286 to 1.256, all exceeding 1.150, with minimal differences and a nearly linear decrease, indicating that they are all in a basically stable state. The possible reason is that as the thickness of the fully weathered soil layer increases, the infiltration depth of rainfall increases. However, the permeability coefficient of the internal soil is relatively small, so after a period of rainfall, the infiltration depth of the soil does not vary significantly. Therefore, the stability coefficients under various conditions are roughly similar after 5 days of rainfall and tend to stabilize. Based on this, it can be inferred that under no rainfall conditions, for terraced slopes, areas with thinner fully weathered soil layers exhibit greater slope stability. During prolonged rainfall, the stability of terraced slopes with varying soil layer thicknesses tends to converge.

Table 1: The slope stability coefficient curve of the slope of the terrace

Soil thickness	Stability factor
1m	1.286
2m	1.273
3m	1.267
4m	1.262
5m	1.256

The overall slope of terraced fields during rainfall has a significant impact on their stability. After 5 days of rainfall, the slope stability coefficients of terraced fields with different slopes vary greatly within the range of 0.985 to 1.629, while those with different soil layer thicknesses vary only slightly within the range of 1.258 to 1.283. Therefore, it can be concluded that under the same rainfall intensity, the overall slope of the terraced fields has a greater impact on stability than the thickness of the soil layers.

III. Slope stability prediction

III. A. Dataset

III. A. 1) Database Establishment

Research indicates that the primary factors influencing slope safety factor include severity γ, cohesion c, internal friction angle φ, slope angle α, slope height H, and pore pressure ratio r_u. Therefore, a sample database was established using six factors from 200 slope cases, with some sample data shown in Table 2.

Table 2: original sample database

Density / (kM.m-3)	Cohesion (MPa)	Internal friction angle /(°)	Slope Angle (°)	Slope height /m	Pore water pressure ratio	safety factor
20.1	27	0	31	9	0.17	1.11
27	48	37	48	446	0.27	1.32
27	58	39	46.4	297	0.27	1.55
29	41	37	48.4	289	0.27	1.14
29	36	37	43	357	0.27	1.29
12	40.13	22.45	0.95	31.3	0.72	1.04
53	47	22	0	38	0.72	0.81
22	0	39	47	52	0.27	0.81
20	32	37	37	13	0.27	2.04
20.54	12.84	22	24	14.09	0.23	1.37
…	…	…	…	…	…	…
27	48	37	49	447	0.27	1.30

III. A. 2) Feature correlation analysis

First, a feature correlation analysis is performed on the selected sample database. If there is correlation between features, dimension reduction is required during prediction to prevent the correlation between features from affecting the prediction results. MATLAB software is used to plot a Pearson correlation heatmap between features, as shown in Figure 7. There is a certain degree of correlation between pairs of features. The correlation coefficient between

the internal friction angle and the slope angle is the highest, at 0.49, while the correlation coefficients between the remaining pairs of features are all less than 0.5. Therefore, all feature correlation coefficients are less than 0.5, indicating that the correlation between features is non-strong, with a noticeable nonlinear relationship. Consequently, no dimensionality reduction is required for the data.

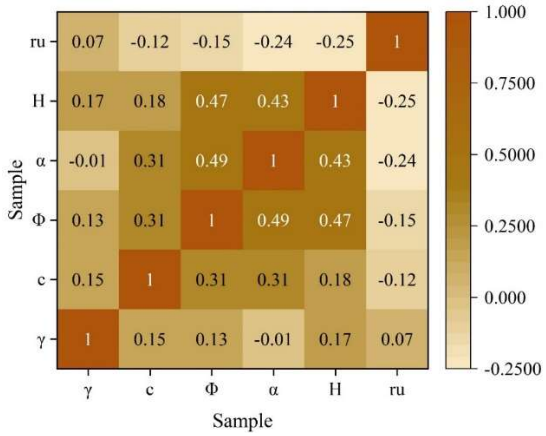

Figure 7: Pearson's correlation heatmap

III. B. Construction of the INGO RF hybrid prediction model

III. B. 1) Random Forest Model

The RF model [25] is an ensemble algorithm that achieves optimal classification through voting by multiple decision trees. First, the Bootstrap method is used to randomly sample 80% of the data from the slope sample set to construct m training sets. Then, k features are randomly selected from each training set to construct n decision trees. Finally, the n decision trees are tested using the training set to obtain n classification results, and slope stability predictions are made based on the voting principle.

III. B. 2) Improving the Northern Goshawk Algorithm Design

(1) Strategy improvement in the prey identification stage

The classic NGO algorithm randomly selects prey to guide population updates in the prey identification stage, which may lead to blindness and local optima. Therefore, this paper makes the following improvements to the algorithm for this stage.

Let F_i and F_{P_i} be the fitness of the i th northern goshawk and its prey, respectively. (1) When $F_i > F_{P_i}$, the northern goshawk has a lower fitness. In this case, the best value of the current individual in each generation is used to guide position updates, which helps accelerate convergence and improve optimization accuracy. (2) When $F_i \le F_{P_i}$, the northern goshawk has a better fitness. At this point, a subtraction optimizer is introduced to adjust the position of the current northern goshawk based on the position difference of all northern goshawks, thereby avoiding the original goshawk getting stuck in a local optimum and balancing global and local information to enhance the algorithm's exploration capability. The improved expression for this stage is:

$$X = \begin{pmatrix} X_1 \\ \vdots \\ X_i \\ \vdots \\ X_N \end{pmatrix} = \begin{pmatrix} x_{1,1} & \cdots & x_{1,j} & \cdots & x_{1,n} \\ \vdots & & \vdots & & \vdots \\ x_{i,1} & \cdots & x_{i,j} & \cdots & x_{i,n} \\ \vdots & & \vdots & & \vdots \\ x_{N,1} & \cdots & x_{N,j} & \cdots & x_{N,n} \end{pmatrix}_{N\times n} \quad x_{best} \tag{6}$$

$$P_i = X_k \quad i = 1,2,\cdots,N \quad k = 1,2,\cdots,i-1,\cdots,N \tag{7}$$

$$x_{i,j}^{new,P1} = \begin{cases} x_{i,j} + r\left(x_{best} - bx_{i,j}\right) & F_{P_i} < F_i \\ x_{i,j} + \dfrac{r}{N}\sum_{k=1}^{N}\left(x_{i,j} - vx_{k,j}\right) & F_{P_i} \ge F_i \end{cases} \tag{8}$$

$$X_i = \begin{cases} X_i^{new,P1} & F_i^{new,P1} < F_i \\ X_i & F_i^{new,P1} \geq F_i \end{cases} \tag{9}$$

In the equation, X is the northern goshawk population matrix, X_i is the position of the i th northern goshawk, N is the population size of northern goshawks, n is the dimension of the problem variables, P_i is the prey position of the i th northern goshawk, $x_{i,j}$ is the position of the i th goshawk in the j th dimension, $X_i^{new,P1}$ is the new position of the i th northern goshawk, $x_{i,j}^{new,P1}$ is the new position of the i th northern goshawk in the j th dimension after the first stage update, x_{best} is the best position of each generation of northern goshawks, r is a random factor, $r \in [0,1]$, b is the position gain, taken as 1 or 2, v is the weight factor, $v \in [1,3]$, and $F_i^{new,P1}$ is the fitness of the i th northern eagle after the first stage update.

(2) Strategy improvement in the pursuit and escape stages

The classic NGO algorithm tends to search for better solutions near the current solution during the pursuit and escape phase, but premature development can easily lead to local optima, especially in complex slope datasets. As the number of algorithm iterations increases, the algorithm eventually converges near the solution. At this point, to improve the quality of the solution, a more detailed search should be conducted within a smaller range. Therefore, for this phase, the following improvements were made to the algorithm: (1) Introduce random perturbations via Cauchy mutation to cause individuals to jump away from local optima, thereby increasing the likelihood of exploring global optima: (2) Design a dynamic update strategy for search upper and lower bounds, dynamically adjusting the search range of individuals through algorithm iterations. In the later stages of the algorithm, as the number of iterations increases, the region around the solution can be explored more thoroughly, thereby improving solution quality. The specific improved expression is:

$$x_{i,j}^{new,P2} = \begin{cases} x_{best} + x_{best} cauchy(0,1) & r_a < \sigma \\ x_{i,j} + \dfrac{R(2r-1)(u_b - l_b)}{t} & r_a \geq \sigma \end{cases} \tag{10}$$

$$R = 0.02(1 - t/T) \tag{11}$$

$$X_i = \begin{cases} X_i^{new,P2} & F_i^{new,P2} < F_i \\ X_i & F_i^{new,P2} \geq F_i \end{cases} \tag{12}$$

where $X_i^{new,P2}$ is the new position of the first i northern goshawk, $x_{i,j}^{new,P2}$ is the new position of the j dimension of the first i northern goshawk after the second stage update, $F_i^{new,P2}$ is the fitness of the first i northern goshawk after the second stage update, $cauchy(0,1)$ is the probability factor in the Cauchy distribution, t is the current number of iterations, T is the maximum number of iterations, R is the scaling factor, its value decreases with the increase of the number of iterations, r_a is the random number of the $[0,1]$ interval, σ is the probability parameter, take 0.2, u_b and l_b The difference between the upper and lower bounds of the variables in the search space decreases with the increase of the number of iterations, forcing the search of the solution to be near the current optimal solution, which can effectively improve the convergence speed and quality of the algorithm.

III. B. 3) INGO RF prediction model establishment process

Since the number of decision trees $n_{estimators}$ and the maximum number of separating features $N_{\max\_features}$ directly affect the classification performance and stability of the RF model, the INGO algorithm is used to tune the hyperparameters of the RF model to improve the prediction accuracy of the model. The block diagram of the prediction model proposed in this paper is shown in Figure 8.

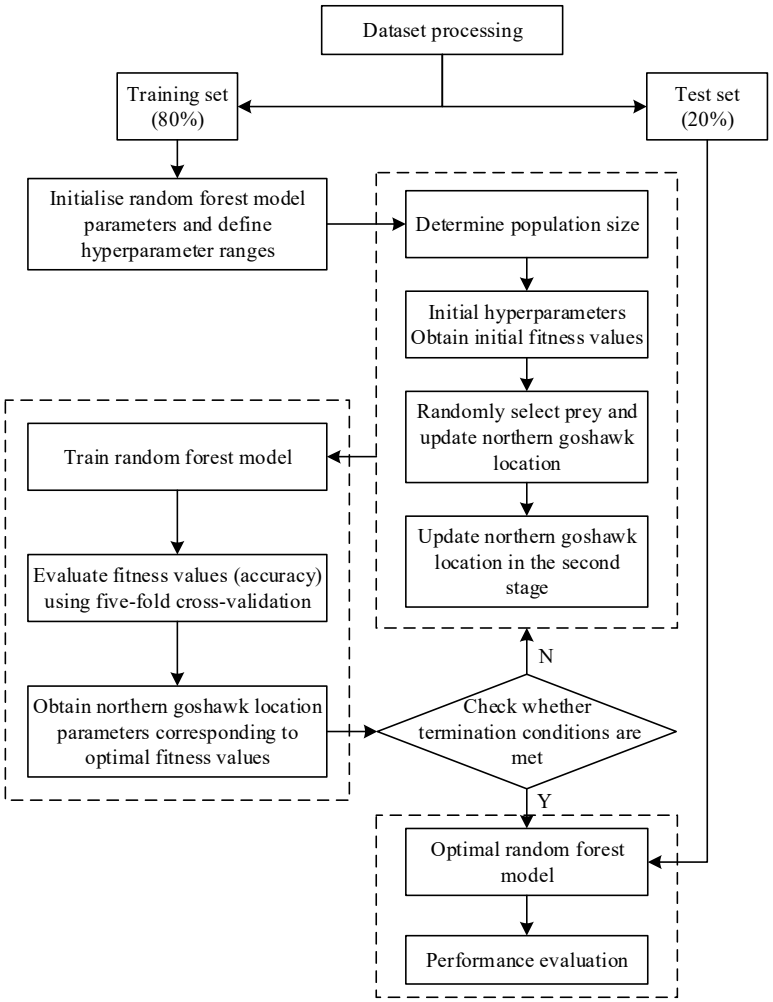

Figure 8: Flowchart of INGO RF slope prediction model

(1) Analyze and normalize the slope dataset, and randomly divide it into a training set and a test set in an 8:2 ratio.

(2) Initialize the parameters of the RF algorithm and determine the search range for the hyperparameters to be tuned.

(3) Initialize the parameters of the INGO algorithm and set the population size.

(4) Perform position iteration updates according to steps (1) to (7).

(5) Use the training set for five-fold cross-validation as the fitness function to verify the fitness of each generation of individuals.

(6) After reaching the maximum number of iterations, output the optimal hyperparameters to construct the optimal INGO RF slope prediction model, and test it using the test set data. The optimal hyperparameter settings for the RF model are shown in Table 3.

(7) Evaluate the performance of the optimal INGO RF prediction model.

Table 3: Optimal hyperparameter settings for the RF model

Hyperparameter	$n_{estimators}$	$N_{\max\_features}$
Optimization range	[1,530]	[1,8]
Optimal value	152	5

III. C. Results and Discussion

III. C. 1) Model Classification Performance Metrics

This study selected five metrics to evaluate the classification performance of the model, namely accuracy (A_{cc}), precision (P_{re}), recall (R_e), the weighted average of precision and recall ($F_{1\text{-}score}$), and the area under the receiver operating characteristic curve (ROC) (AUC). The expressions for the first four are as follows:

$$A_{cc} = \frac{T_p + T_n}{T_p + F_n + F_p + T_n} \tag{13}$$

$$P_{re} = \frac{T_p}{T_p + F_p} \tag{14}$$

$$R_e = \frac{T_p}{T_p + F_n} \tag{15}$$

$$F_{1\text{-}score} = \frac{2P_{re}R_e}{P_{re} + R_e} \tag{16}$$

Accuracy is one of the most basic performance metrics for classification models, representing the proportion of correct predictions made by the model. Precision is the proportion of true positives among the model's positive predictions, while recall is the proportion of correct positive predictions made by the model. The $F_{1\text{-}score}$ is a comprehensive metric for evaluating the classification performance of a model.

The expressions for the false positive rate (F_{pr}) and true positive rate (T_{pr}) are:

$$F_{pr} = \frac{F_p}{F_p + T_n} \tag{17}$$

$$T_{pr} = \frac{T_p}{T_p + F_n} \tag{18}$$

The ROC curve is a curve with the false positive rate as the x-axis and the true positive rate as the y-axis. Based on the predicted probability and actual label, F_{pr} and T_{pr} at different thresholds are plotted in the coordinate system, and the points are connected to form the ROC curve. The closer the ROC curve is to the upper left corner, the better the model performance. The AUC value is a comprehensive metric for evaluating the classification performance of a model, with a range from 0 to 1. The closer the AUC value is to 1, the better the model performance.

III. C. 2) INGO-RF model prediction results

The training set and test set were input into the optimal WOA-RF model, and the confusion matrices and classification performance metrics for the training and testing results are shown in Figure 9, while the ROC curves are shown in Figure 10. From the confusion matrix, it can be seen that in the training set and test set, there are 1 and 3 stable samples, respectively, that were incorrectly predicted as unstable, but all unstable samples were correctly predicted. Therefore, the established hybrid model has good performance in identifying slope instability and meets engineering requirements. Calculating the classification performance metrics yields the following results: on the training set, the model's A_{cc} is 0.98, P_{re} is 1.00, R_e is 0.97, and the AUC value is 0.98, indicating that the model's training performance is good. On the test set, the model's A_{cc} is 0.95, P_{re} is 1.00, R_e is 0.86, and the AUC value is 0.97, indicating that the model's generalization performance is good.

(a) Training set, A_{cc} =0.98, P_{re} =1, R_e =0.97, $F_{1-score}$ =0.98 (b) Test set, A_{cc} =0.95, P_{re} =1, R_e =0.86, $F_{1-score}$ =0.93

Figure 9: Confusion matrix and classification performance of model for training and test sets

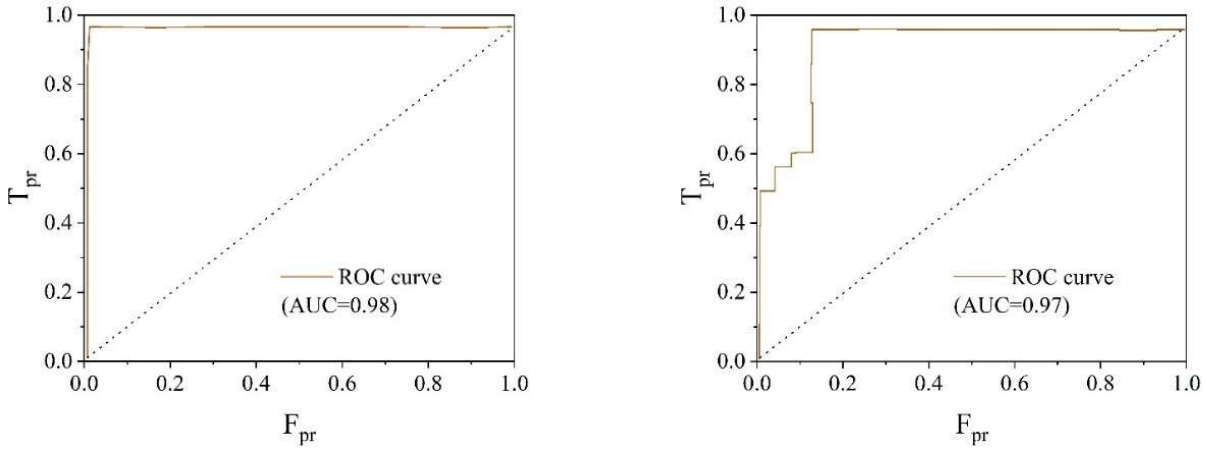

(a) Training set (b) Test set

Figure 10: ROC curves of model for training and test sets

III. C. 3) Comparative analysis of different classification models

To further explore the feasibility of INGO optimization hyperparameters and the predictive performance of the INGO RF model, the INGO optimization algorithm was used to optimize four widely used machine learning models (k-nearest neighbors algorithm (KNN), SVM, ANN, and DT). The optimized models will be compared and analyzed with the INGO RF model. All these models will be trained using the training set and evaluated using the test set. The training and test sets for these models will be consistent with those of the INGO RF model to ensure the reliability of the results.

Table 4 shows the A_{cc} and $F_{1-score}$ values for each model before and after optimization on the test set. It can be seen that after INGO optimization, the A_{cc} and $F_{1-score}$ of all models have been improved to varying degrees, indicating that INGO can achieve hyperparameter optimization and performance improvement for the four machine learning models. Among them, the ANN model shows the highest improvement, with both A_{cc} and $F_{1-score}$ increasing by 0.27. The INGO RF model's A_{cc} and $F_{1-score}$ are both 0.95, representing a 12.4% improvement in both metrics compared to the RF model. The performance of the RF model before and after optimization is superior to that of the other four models before and after optimization.

Table 4: A_{cc} and $F_{1-score}$ before and after optimization

Model	A_{cc}	$F_{1-score}$	Model	A_{cc}	$F_{1-score}$
KNN	0.77	0.77	INGO- KNN	0.85	0.85
SVM	0.82	0.82	INGO-SVM	0.87	0.86
ANN	0.54	0.53	INGO-ANN	0.81	0.80
DT	0.73	0.73	INGO-DT	0.77	0.77
RF	0.86	0.86	INGO-RF	0.95	0.95

Table 5 presents the classification performance metrics of each optimized model on the test set. Models are ranked based on their performance across each metric, with higher performance corresponding to a larger rank value. The rank values for the four metrics are summed to obtain the total score. As shown in Table 4, the total scores of the five optimized models, from highest to lowest, are INGO-RF (24), INGO-SVM (20), INGO-KNN (15), INGO-ANN (9), and INGO-DT (4). Since INGO-RF and INGO-SVM have relatively high total scores, they can effectively predict slope stability. Additionally, INGO-RF's total score is significantly higher than INGO-DT's, indicating that integrating RF with DT can significantly enhance the model's predictive performance.

Table 5: Classification performance and ranking of models after optimization

Model	A_{cc}	A_{cc} rank	P_{re}	P_{re} rank	R_e	R_e rank	$F_{1-score}$	$F_{1-score}$ rank	Total score
INGO- KNN	0.84	4	0.84	3	0.84	4	0.84	4	15
INGO-SVM	0.86	5	0.87	5	0.86	5	0.86	5	20
INGO-ANN	0.82	2	0.85	3	0.78	2	0.81	2	9
INGO-DT	0.77	1	0.77	1	0.74	1	0.75	1	4
INGO-RF	0.96	6	1.00	6	0.89	6	0.95	6	24

Figure 11 shows the ROC curves and AUC values of each model on the test set. It can be observed that no single model's ROC curve completely encompasses those of the other models. The ROC curves of the INGO-RF, INGO-KNN, and INGO-SVM models are closer to the top-left corner, with AUC values of 0.954, 0.867, and 0.849, respectively. The INGO-RF model has the highest AUC value, exceeding 0.9. Therefore, the INGO-RF model demonstrates the best predictive performance.

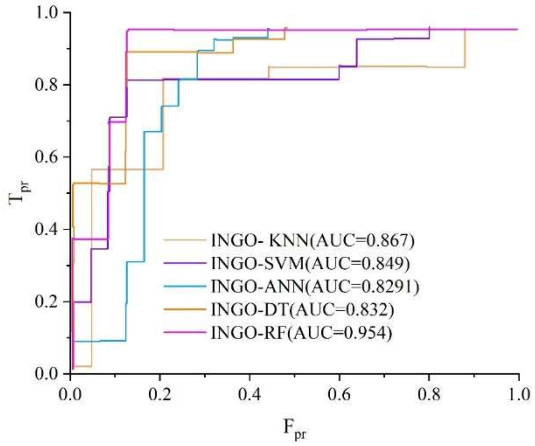

Figure 11: ROC curves of different models for the test set

In addition, to comprehensively evaluate the classification performance of each model, a radar chart was drawn based on the above five indicators, as shown in Figure 12. The results show that the constructed INGO-RF model outperforms other models in all indicators, demonstrating excellent performance. Therefore, the INGO-RF model is selected as the best model for predicting slope stability.

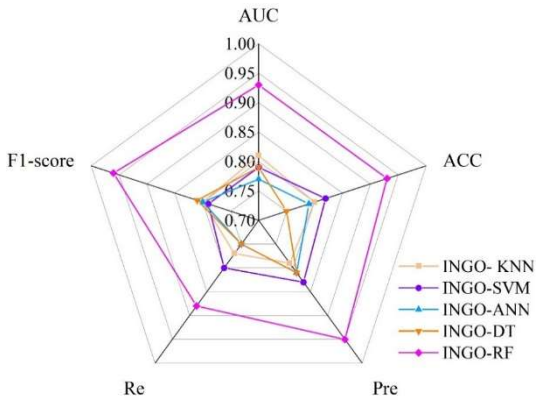

Figure 12: Radar chart of performance indicators for different models

III. C. 4) Feature Importance Analysis

Exploring feature importance and determining its impact on slope stability is crucial, as the analysis results can provide a basis for slope prevention and control. The PFI algorithm is used to assess feature importance by randomly shuffling the feature value sequence and calculating the degree of model performance degradation.

Multiple feature importance analyses are performed on the trained INGO-RF model to obtain the mean and standard deviation of the feature weight coefficients, as shown in Figure 13.

In the figure, the main predictive feature indicators are the cohesion γ, cohesion coefficient c, internal friction angle φ, slope angle α, slope height H, and pore pressure ratio r_u. Clearly, γ (with an average weight coefficient of 0.165) is the most sensitive factor affecting slope stability. The average weight coefficients of H, Φ, r_u and ϕ have similar mean weight coefficients of 0.105, 0.094, 0.085, 0.079, and 0.067, respectively. Therefore, the importance of the features, from highest to lowest, is: γ, H, Φ, r_u and ϕ. These features all play an important role in slope stability and are reasonable inputs for the model.

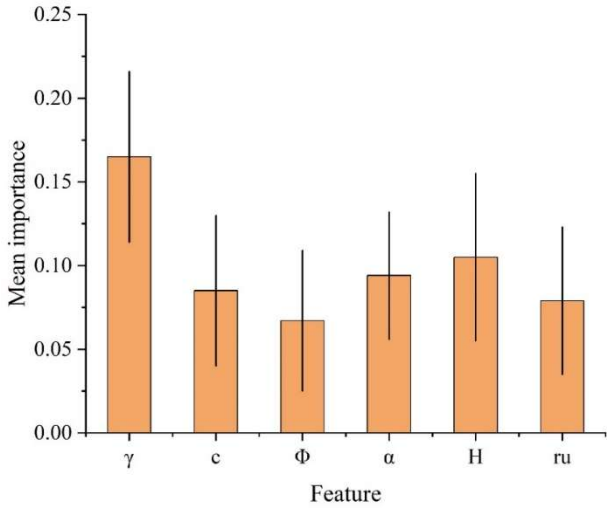

Figure 13: Feature importance score (iteration: 100)

IV. Conclusion

A computational model was established using numerical simulation based on the strength reduction method, with the Ball-Wall method selected for modeling. The concept of contact adhesion was incorporated into the model to analyze the impact of different soil layer thicknesses on the stability of terraced slopes. The results showed that thinner soil layers lead to better slope stability, and as the rainfall infiltration process continues, the influence of soil layer thickness on slope stability gradually decreases. Subsequently, a prediction model based on the INGO algorithm for optimizing RF hyperparameters was proposed. Among the five hybrid ensemble models constructed—INGO-KNN, INGO-SVM, INGO-ANN, INGO-DT, and INGO-RF—the INGO-RF model exhibited the best classification performance metrics and overall performance. The feature weight coefficient of γ was the largest, indicating its greatest influence on slope stability.

References

[1] Basahel, H., & Mitri, H. (2017). Application of rock mass classification systems to rock slope stability assessment: A case study. Journal of rock mechanics and geotechnical engineering, 9(6), 993-1009.

[2] Igwe, O., & Chukwu, C. (2019). Slope stability analysis of mine waste dumps at a mine site in Southeastern Nigeria. Bulletin of Engineering Geology and the Environment, 78, 2503-2517.

[3] Wang, Y., Zhang, Z., Kang, X., Xie, H., Wang, C., & Liu, K. (2024). Stability Analysis of Soil and Rock Mixed Slope Based on Random Heterogeneous Structure. Advances in Civil Engineering, 2024(1), 1448371.

[4] Zhang, J. (2022). Intelligent identification of rock mass structural plane and stability analysis of rock slope block. Scientific Reports, 12(1), 16745.

[5] Zhang, H., Wu, S., Zhang, Z., & Huang, S. (2023). Reliability analysis of rock slopes considering the uncertainty of joint spatial distributions. Computers and Geotechnics, 161, 105566.

[6] Pan, Q., Xu, J., & Dias, D. (2017). Three-dimensional stability of a slope subjected to seepage forces. International Journal of Geomechanics, 17(8), 04017035.

[7] Massey, C., Della Pasqua, F., Holden, C., Kaiser, A., Richards, L., Wartman, J., ... & Janku, L. (2017). Rock slope response to strong earthquake shaking. Landslides, 14, 249-268.

[8] Sun, J., Huang, C. H., Han, G., & Wang, Y. (2019). Effects of cover on soil particle and associated soil nutrient redistribution on slopes under rainfall simulation. Journal of Soils and Sediments, 19, 729-740.

[9] Song, X., Tan, Y., & Lu, Y. (2024). Microscopic analyses of the reinforcement mechanism of plant roots in different morphologies on the stability of soil slopes under heavy rainfall. Catena, 241, 108018.

[10] Nakajima, S., Abe, K., Shinoda, M., Nakamura, S., Nakamura, H., & Chigira, K. (2019). Dynamic centrifuge model tests and material point method analysis of the impact force of a sliding soil mass caused by earthquake-induced slope failure. Soils and Foundations, 59(6), 1813-1829.
[11] Liu, G. W., Song, D. Q., Chen, Z., & Yang, J. W. (2020). Dynamic response characteristics and failure mechanism of coal slopes with weak intercalated layers under blasting loads. Advances in Civil Engineering, 2020(1), 5412795.
[12] Chen, H. E., Tsai, T. L., & Yang, J. C. (2017). Threshold of slope instability induced by rainfall and lateral flow. Water, 9(9), 722.
[13] Mengistu, F., Suryabhagavan, K. V., Raghuvanshi, T. K., & Lewi, E. (2019). Landslide Hazard zonation and slope instability assessment using optical and InSAR data: a case study from Gidole town and its surrounding areas, southern Ethiopia. Remote Sensing of Land, 3(1), 1-14.
[14] Chiarelli, D. D., D'Odorico, P., Davis, K. F., Rosso, R., & Rulli, M. C. (2021). Large‐scale land acquisition as a potential driver of slope instability. Land Degradation & Development, 32(4), 1773-1785.
[15] Conforti, M., & Ietto, F. (2019). An integrated approach to investigate slope instability affecting infrastructures. Bulletin of Engineering Geology and the Environment, 78, 2355-2375.
[16] He, J., Wang, S., Liu, H., Nguyen, V., & Han, W. (2021). The critical curve for shallow saturated zone in soil slope under rainfall and its prediction for landslide characteristics. Bulletin of Engineering Geology and the Environment, 80, 1927-1945.
[17] Sinchith, M., Nandi, S., & Ghosh, P. (2023). Critical stability analysis of slopes using stress characteristics in purely cohesive soil. International Journal of Geomechanics, 23(1), 04022263.
[18] Sertabipoğlu, Z., Özer, Ü., & Tunçdemir, H. (2020). Assessment of slope instability with effects of critical displacement by using InSAR and FEM. Arabian Journal of Geosciences, 13, 1-15.
[19] Demir, S., & Sahin, E. K. (2023). Application of state-of-the-art machine learning algorithms for slope stability prediction by handling outliers of the dataset. Earth Science Informatics, 16(3), 2497-2509.
[20] Lin, Y., Zhou, K., & Li, J. (2018). Prediction of slope stability using four supervised learning methods. Ieee Access, 6, 31169-31179.
[21] Li, M., Li, K., Qin, Q., & Yue, R. (2023). Slope stability prediction based on IPOARF algorithm: A case study of Lala Copper Mine, Sichuan, China. Expert Systems with Applications, 229, 120595.
[22] Meng, J., Mattsson, H., & Laue, J. (2021). Three‐dimensional slope stability predictions using artificial neural networks. International Journal for Numerical and Analytical Methods in Geomechanics, 45(13), 1988-2000.
[23] Lin, M., Zeng, L., Teng, S., Chen, G., & Hu, B. (2024). Prediction of stability of a slope with weak layers using convolutional neural networks. Natural Hazards, 120(13), 12081-12105.
[24] SeyedSaber Hosseini,Farshad Astaraki,Seyed Mohammad Reza Imam,Jafar Chalabii & Majid Movahedi Rad. (2024). Investigation of Shear Strength Reduction Method in Slope Stability of Reinforced Slopes by Anchor and Nail. Buildings,14(2),
[25] Jian Zhou,Zijian Liu,Chuanqi Li,Kun Du & Haiqing Yang. (2025). Cutting-edge approaches to specific energy prediction in TBM disc cutters: Integrating COSSA-RF model with three interpretative techniques. Underground Space,22,241-262.